



Aalborg Universitet

AALBORG UNIVERSITY
DENMARK

The Transformation from Translucent into Transparent Rare Earth Ions Doped Oxyfluoride Glass-Ceramics with Enhanced Luminescence

Li, Zhencai; Chen, C.Y.; Shen, W.H.; Zhou, D.C.; Jensen, Lars Rosgaard; Qiao, X.S.; Ren, J.J.; Du, J.C.; Zhang, Y.F.; Qiu, J.B.; Yue, Yuanzheng

Published in:
Advanced Optical Materials

DOI (link to publication from Publisher):
[10.1002/adom.202102713](https://doi.org/10.1002/adom.202102713)

Creative Commons License
CC BY-NC 4.0

Publication date:
2022

Document Version
Publisher's PDF, also known as Version of record

[Link to publication from Aalborg University](#)

Citation for published version (APA):

Li, Z., Chen, C. Y., Shen, W. H., Zhou, D. C., Jensen, L. R., Qiao, X. S., Ren, J. J., Du, J. C., Zhang, Y. F., Qiu, J. B., & Yue, Y. (2022). The Transformation from Translucent into Transparent Rare Earth Ions Doped Oxyfluoride Glass-Ceramics with Enhanced Luminescence. *Advanced Optical Materials*, 10(13), Article 2102713. <https://doi.org/10.1002/adom.202102713>

General rights

Copyright and moral rights for the publications made accessible in the public portal are retained by the authors and/or other copyright owners and it is a condition of accessing publications that users recognise and abide by the legal requirements associated with these rights.

- Users may download and print one copy of any publication from the public portal for the purpose of private study or research.
- You may not further distribute the material or use it for any profit-making activity or commercial gain
- You may freely distribute the URL identifying the publication in the public portal -

Take down policy

If you believe that this document breaches copyright please contact us at vbn@aub.aau.dk providing details, and we will remove access to the work immediately and investigate your claim.

The Transformation from Translucent into Transparent Rare Earth Ions Doped Oxyfluoride Glass-Ceramics with Enhanced Luminescence

Zhencai Li, Chunying Chen, Weihui Shen, Dacheng Zhou, Lars R. Jensen, Xvsheng Qiao, Jinjun Ren, Jincheng Du, Yanfei Zhang, Jianbei Qiu,* and Yuanzheng Yue*

It is known that the optical transparency of an oxide glass decreases with an increase in the size and fraction of crystals in the glass during heat-treatment. Here, the authors report an opposite scenario, where a translucent $\text{Er}^{3+}\text{-Yb}^{3+}$ doped oxyfluoride precursor glass-ceramic (P-GC) becomes transparent with increasing crystal size and crystallinity. Specifically, in the heat-treated P-GC samples, the authors observe that the growth of the existing Ba_2LaF_7 crystals and particularly the formation of small spherical Ba_2LaF_7 crystals greatly enhanced the light transmittance. To reveal the origin of this anomalous phenomenon, the authors perform detailed morphology and structure analyses on both P-GC and the heat-treated P-GC samples and molecular dynamics simulations of the precursor glass. The results show that the composition of the residual glass phase is altered (e.g., depletion of La^{3+}) in the way that the differences in refractive index between the glass matrix and the crystals are greatly reduced. As a consequence, the light scattering of the heat-treated P-GC is suppressed, and hence, the derived P-GC becomes transparent. In addition, a proper heat-treatment can also enhance the luminescence of the studied P-GC system.

in the oxide glass matrix.^[1,2] This material bears the advantages of both the fluoride crystallites and the oxide glass matrix.^[3] The crystallites have a low phonon energy environment, while the oxide glass matrix possesses both high optical transparency and excellent chemical and thermal stabilities, which are crucial for protecting the fluoride crystallites from reacting with the moisture from the environment. For the oxyfluoride GCs doped with rare earth (RE) ions, the RE ions, which serve as the up-conversion (UC) luminescence centers, preferentially enter the fluoride crystallites, and hence, reduce the rate of nonradiative relaxation, thereby benefiting the UC luminescence.^[4] Thus, oxyfluoride GCs are a promising candidate for optical applications such as optical amplifiers,^[5] multicolor displays,^[6] UC fibers,^[7] lasers,^[8] and optical thermometry.^[9] However, it is a challenge to achieve the oxyfluoride GCs

with both high transparency and superior UC luminescence.


Usually, the optical transmittance of the oxyfluoride GCs is lower than that of their corresponding precursor glass since the former has stronger optical absorption and light scattering

1. Introduction

Traditional oxyfluoride glass-ceramics (GCs) are a kind of multiphase material that contain fluoride crystallites embedded

Z. Li, Y. Yue
Department of Chemistry and Bioscience
Aalborg University
Aalborg DK-9220, Denmark
E-mail: yy@bio.aau.dk

C. Chen, J. Ren
Shanghai Institute of Optics and Fine Mechanics
Chinese Academy of Sciences
Shanghai 201800, China

 The ORCID identification number(s) for the author(s) of this article can be found under <https://doi.org/10.1002/adom.202102713>.

© 2022 The Authors. Advanced Optical Materials published by Wiley-VCH GmbH. This is an open access article under the terms of the Creative Commons Attribution-NonCommercial License, which permits use, distribution and reproduction in any medium, provided the original work is properly cited and is not used for commercial purposes.

DOI: 10.1002/adom.202102713

W. Shen, D. Zhou, J. Qiu
School of Material Science and Engineering
Kunming University of Science and Technology
Kunming 650093, China
E-mail: qiu@kmust.edu.cn

L. R. Jensen
Department of Materials and Production
Aalborg University
Aalborg DK-9220, Denmark

X. Qiao
School of Materials Science and Engineering
Zhejiang University
Hangzhou 310027, China

J. Du
Department of Materials Science and Engineering
University of North Texas
Denton, TX 76203, USA

Y. Zhang
School of Materials Science and Engineering
Qilu University of Technology
Jinan 250353, China

than the latter. According to the Rayleigh–Gans theory,^[10] if crystallinity is low (e.g., <40 vol.% and the average size of the fluoride crystallites is well below the wavelength of the incident light, the light scattering in the visible range will be low. If the average size of fluoride crystallites is less than 30 nm, most of the oxyfluoride GCs would exhibit ultrahigh transparency owing to less light scattering and absorption.^[11] But on the other hand, if the fluoride crystallites are too small, they will not accommodate a large amount of RE ions required to achieve high UC luminescence efficiency.^[12–14] Therefore, it is important to find a way to realize both high transparency and superior UC luminescence efficiency in the same material. To do so, it is necessary to tailor the chemical composition and size of crystallites in the oxide glass matrix.

By altering the concentration of glass modifiers in the chemical composition, we have found several translucent oxyfluoride GCs obtained via quenching glass melts, which contain large (>100 μm) fluoride crystals. In addition, the strategy of isothermal heat-treatment (HT) can be used to adjust the refractive index (*n*) of the glass matrix to match that of the fluoride crystals, thereby increasing the transparency of the translucent samples by minimizing the *n* difference (<0.01) between the fluoride crystallites and the glass matrix. In this work, we investigate one of the above-mentioned translucent oxyfluoride GCs, i.e., 45SiO₂-15Al₂O₃-12Na₂O-21BaF₂-7LaF₃-0.5ErF₃-1.0YbF₃, to demonstrate the translucency-to-transparency transformation caused by a proper HT process.

To determine the structure, size, and fraction of the crystals in the oxyfluoride GCs, we performed high-resolution transmission electron microscopy (HRTEM), scanning electron microscopy (SEM), and X-ray diffraction (XRD). To study both the crystal formation and the glass transition of the GCs, we conducted differential scanning calorimetry (DSC) and XRD. In the end, we achieved the match of the *n* of the glass matrix with that of the crystal phase, and thereby the high transparency of the oxyfluoride GCs. The origin of the HT enhancement of transparency of the oxyfluoride GCs was clarified by the solid-state nuclear magnetic resonance (NMR) and the Raman spectroscopy, as well as the molecular dynamics (MD) simulation. Furthermore, the optimized HT condition resulted in superior luminescence efficiency.

2. Results and Discussion

2.1. Optical, Thermal, and Structural Analyses

Figure 1a shows the optical transmittance of both precursor glass-ceramic (P-GC) and three heat-treated P-GC samples, which are derived from their absorption spectra in the wavelength range of 275 to 800 nm (Figure S2a, Supporting Information).^[14] It is seen that the transmittance increases with the HT temperature. The trend can also be reflected by the optical images of P-GC and the three P-GC samples heat-treated at 600,

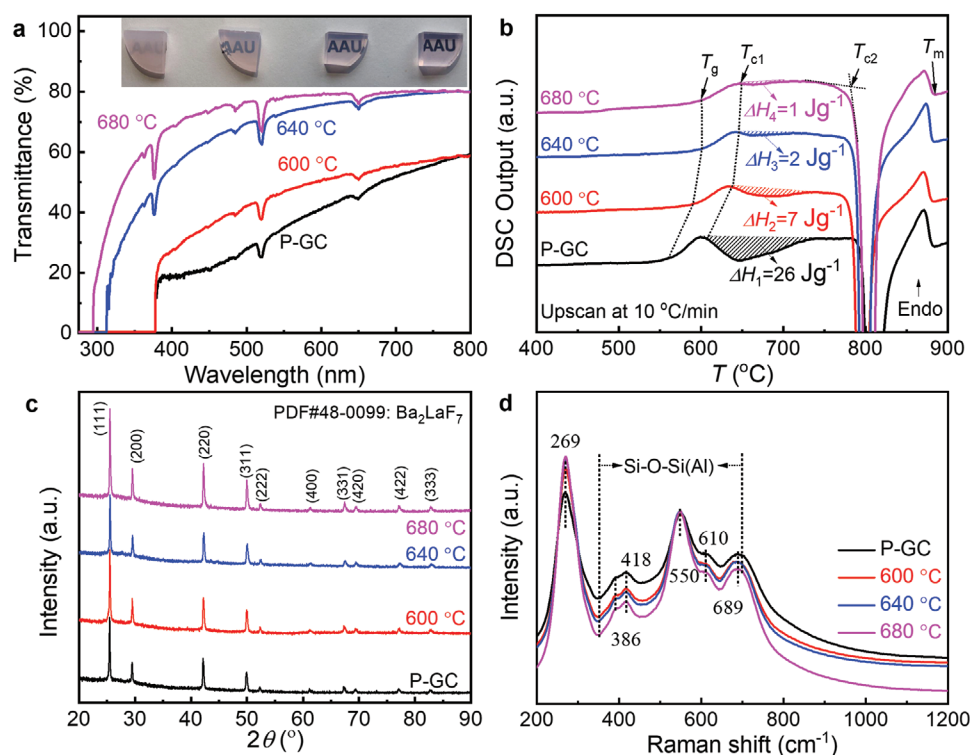


Figure 1. Impact of HT on optical and structural characteristics of P-GC. a) Transmittance of P-GC before and after HT at 600, 640, and 680 °C for 4 h. Inset: Photos of P-GC sample and P-GC samples heat-treated at 600, 640, and 680 °C for 4 h, respectively (from left to right). b) DSC output (arbitrary unit) of P-GC and the heat-treated P-GC samples. The glass transition temperatures (T_g), the onset temperatures of both the first and second crystallization peaks (T_{c1} and T_{c2} , respectively), and the offset temperature of the melting peak, i.e., the melting point (T_m) (see the arrows). Hatched area: crystallization enthalpy. c) XRD patterns. d) Normalized Raman spectra, where the vibrational modes and the peak positions are indicated.

640, and 680 °C (from left to right, respectively) for 4 h (Inset of Figure 1a). The increase in the transmittance can be clarified as follows. First, the average size of the Ba₂LaF₇ nanocrystals decreases with the increasing HT temperature. If it is controlled within 30 nm, the light scattering in grain boundaries can be avoided. Second, for large-sized crystals (e.g., up to micrometer scale), both light scattering and absorption can be attenuated by only minimizing the *n* difference (<0.01) between crystals and glass matrix.^[15]

Figure 1b shows the DSC curves of both the P-GC and the three P-GC samples that were heat-treated at 600, 640, and 680 °C for 4 h, respectively. It is seen that P-GC undergoes glass transition with the onset temperature (*T_g*) and the two crystallization processes with the onset temperatures of *T_{c1}* and *T_{c2}*, respectively, and finally the melting with the offset temperature of *T_m*. The values of *T_g*, *T_{c1}*, *T_{c2}*, and *T_m* are determined to be 559, 607, 792, and 871 °C, respectively, by the method described elsewhere.^[16] It is observed in Figure 1b and Table S1 (Supporting Information) that *T_g* and *T_{c1}* first increase with both the HT temperature and duration and then remain unchanged. The maximum *T_g* and *T_{c1}* values indicate that the crystallinity has reached the maximum at a sufficiently high extent of HT. In other words, the composition of the glass matrix phase does not vary with further HT, i.e., the glass structure does not change.^[17] The onset temperature of the main crystallization peak (*T_{c2}*) of P-GC decreases from 792 to 782 °C upon HT at 600 °C for 4 h, and then remains unchanged with further increasing HT temperature. However, the *T_m* value remains constant with increasing HT temperature. To determine the stability of the glass network structure against crystallization, P-GC samples were subjected to 4 cycles of DSC scans up to the maximum scanning temperatures (*T_{scan-max}*) of 580, 600, 620, 640, and 660 °C, respectively, at 10 °C min⁻¹. In Figure S2b and Table S2, (Supporting Information), it is seen that *T_g* first sharply increases and then gradually approaches the highest value by repeating the DSC scans. This implies that the glass network connectivity increases with DSC scans, and reaches a maximum, due to the cease of crystallization.^[18] To study the first crystallization event of both P-GC and the heat-treated P-GC samples, the crystallization enthalpy (ΔH) of each sample was calculated by integrating the exothermic peak (Figure 1b). It is evident that ΔH gradually decreases with increasing HT temperature, implying that the crystallization already takes place during HT. This means that P-GC has a strong tendency to crystallize before the main crystallization occurs at ≈ 800 °C (Figure 1b).^[19]

Figure 1c shows the XRD patterns of both P-GC and three heat-treated P-GC samples. The diffraction peaks of P-GC are identified to be the face-centered cubic (FCC) Ba₂LaF₇ crystal (PDF#48-0099), suggesting that a certain amount of crystals have already formed during melt-quenching.^[20] The intensities of the diffraction peaks increase with HT temperature and no new diffraction peaks appear. To determine the purity of the cubic Ba₂LaF₇ crystals, the XRD Rietveld refinement of the P-GC sample heat-treated at 640 °C for 4 h was performed using TOPAS software. The difference between the observed and calculated plots is shown in Figure S3 (Supporting Information). The cubic Ba₂LaF₇ nanocrystal structure and equivalent isotropic parameters are given in Table S3 (Supporting

Information). It is seen that there is an excellent match between the observed and the calculated plots, suggesting that only the Ba₂LaF₇ crystals are present in the studied samples. From the XRD results, the crystallinity is found to increase from 42 to 64% with increasing the HT temperature up to 680 °C for 4 h (Table S4, Supporting Information). This implies that HT leads to the formation of Ba₂LaF₇ crystals in P-GC.

Figure 1d illustrates the Raman spectra acquired using the 532 nm laser and subsequently normalized by the intensity of the peak at 550 cm⁻¹ for both P-GC and the heat-treated P-GC samples. The mid-frequency bands at 350–700 cm⁻¹ are associated with the Si-O-Si (Al) symmetric stretching vibration mode in the glass matrix.^[21–23] Specifically, the peak at 418 cm⁻¹ is assigned to a symmetric ring-breathing mode (five-fold ring structure) involving mainly oxygen motion, whereas the peaks at 550, and 610 cm⁻¹ are attributed to the symmetric stretch of three-fold ring structures, respectively.^[24,25] Strikingly, a sharp peak in the low-frequency region appears at ≈ 269 cm⁻¹ for P-GC, which is ascribed to the vibration of the Ba-F and La-F bonds in Ba₂LaF₇ crystals.^[25] This confirms that Ba₂LaF₇ crystals have already formed in the precursor glass during melt-quenching compared with the traditional oxyfluoride glasses (Figure S4a, Supporting Information). Furthermore, the normalized intensity of the peak at 269 cm⁻¹ increases with the HT temperature. Other peaks at 386, 416, 550, 616, and 689 cm⁻¹, which are associated with tetrahedral units in glass matrix, become weaker with the HT temperature, verifying an increase of the crystallinity in the studied samples upon HT.

2.2. Evolution of Crystals and Its Structural Origin

Figure 2a–d show the SEM images of both P-GC and the heat-treated P-GC samples. For P-GC, there are three distinct regions: white flower-like, white, and black domains (Figure 2a), which correspond to Ba₂LaF₇ crystals, fluoride-rich glass matrix, and silica-rich glass matrix, respectively. The silica-rich glass matrix contains [SiO₄] and [AlO₄] tetrahedral units. However, La³⁺ ions can be regarded as the network intermediate.^[26] Therefore, a few La³⁺ ions might enter the silica-rich network, forming [Si(La)O₄] tetrahedral units. Both [SiO₄] and [AlO₄] domains in the surface layer were etched by HF acid, so that the contrast between the fluoride-rich phases (see the white domains in Figure 2a) and the remaining silica-rich phases (see black domains) can be seen.^[27] Flower-like Ba₂LaF₇ crystals (180–190 nm) are distributed in the fluoride-rich phases. Ba₂LaF₇ crystals grow to ≈ 220 nm and the tiny spherical Ba₂LaF₇ nanocrystals (≈ 5 nm) precipitate from the fluoride-rich phase upon HT at 600 °C for 4 h (Figure 2b). This implies that the formation of the fluoride-rich phase assists the growth of the existing crystals and the formation of Ba₂LaF₇ nanocrystals. Upon HT at 640 °C for 4 h, both the flower-like crystals and the nanocrystals grow to ≈ 260 and 15 nm, respectively (Figure 2c). At 680 °C for 4 h, two types of Ba₂LaF₇ crystals further grow to 300 and 25 nm, respectively (Figure 2d). This indicates an increase in both the crystallinity and the average size of the flower-like Ba₂LaF₇ crystals with increasing HT temperature.

MD simulation is conducted to reveal the glass structural features of P-GC composition, which is then compared with the

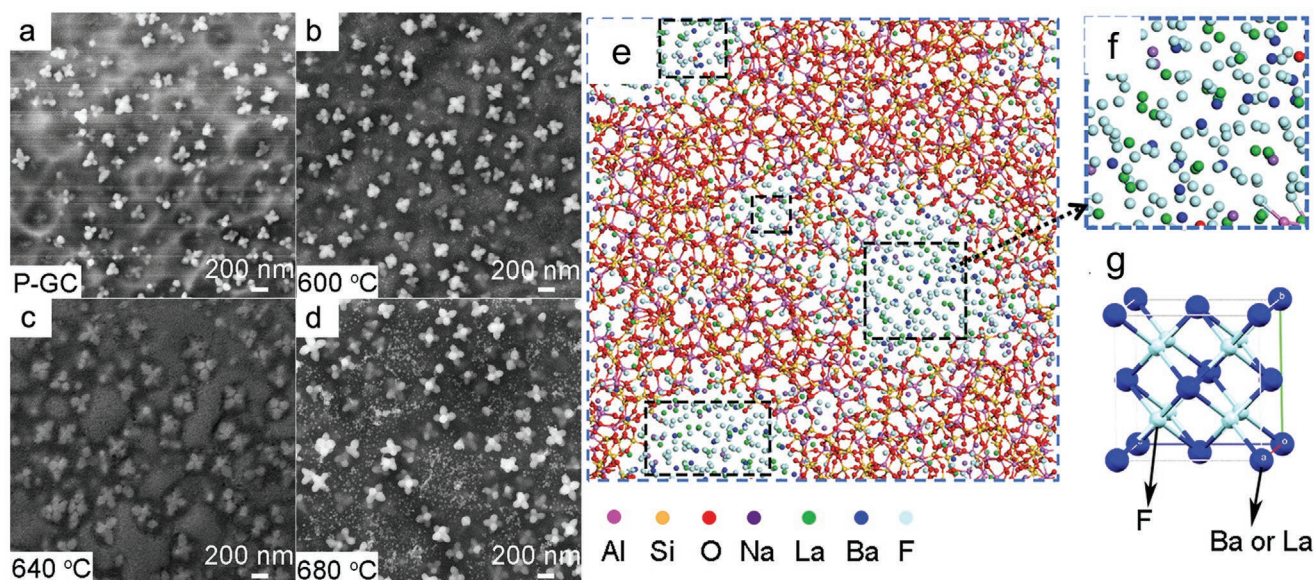


Figure 2. Revealing the structural origin of the crystal evolution by SEM and MD simulation. a–d) The evolution of crystals with HT temperature; e–g) MD simulated structure of P-GC system. a) P-GC; b–d) the three P-GC samples heat-treated at 600, 640, and 680 °C for 4 h, respectively. e) MD simulated structure of P-GC composed of network-forming SiO₄ and AlO₄ tetrahedra and network modifiers. Note that Er³⁺ and Yb³⁺ are replaced by La³⁺ to perform MD simulations. f) A signified structural domain taken from (e), which is enriched in network modifying ions and F⁻ ions. g) Cubic lattice structure of a Ba₂LaF₇ crystallite.

experimentally detected ones. Under the rapid cooling condition of MD simulations, the simulated glass structure shows the regions of the aluminosilicate-rich phase and fluoride-rich phase (Figure 2e), and this is a clear signature of phase separation.^[28] The high tendency of phase separation leads to the occurrence of spontaneous crystallization in the P-GC composition during cooling under the current experimental condition. In addition, the fluoride-rich region detected by MD simulations has a chemical composition similar to that of the fluoride crystals found by energy-dispersive X-ray spectrometer (EDS). As shown in Figure 2e, the oxide-rich phase is composed of a network structure with [SiO₄] and [AlO₄] tetrahedral units linked through corner-sharing of bridging oxygen. In comparison, the fluoride-rich phase is rich in modifier cations, such as Na⁺, Ba²⁺, and La³⁺, with coordination numbers of >4. The structure of the fluoride-rich phase can be described by a polyhedral random packing model or be interpreted by Poulain's ionic glass model (Figure 2f).^[29,30] Al³⁺, Na⁺, Ba²⁺, and La³⁺ ions are preferentially distributed at the interface between oxide- and fluoride-rich phases, and these cations not only act as network modifiers in the silicate phase but also connect the non-bridging O_{1/2}⁻ and ionic F⁻ of fluoride phase.

2.3. Observation of Crystal Evolution at Different Length Scales

Figure 3 shows the micrographs obtained by the aberration-corrected transmission electron microscopy (ACTEM) and HRTEM for both P-GC and the heat-treated P-GC samples. For P-GC (image A in the first row of Figure 3), flower-like Ba₂LaF₇ crystals (≈190 nm) precipitate from the glass matrix. HRTEM image B (taken from the red dotted circle in image A) shows the crystal lattice fringes with the spacings of 0.345 nm

and 0.295 nm that are indexed as the (111) and (220) plane of Ba₂LaF₇ crystals, respectively. The selected area electron diffraction (SAED) photograph (image C) reveals that Ba₂LaF₇ are single crystals. The HRTEM image D (taken from the black dotted box in image A) implies the amorphous nature of the matrix phase. This means that flower-like Ba₂LaF₇ crystals are distributed in the glass matrix of the P-GC sample.

Upon HT at 600 °C, the Ba₂LaF₇ crystals grow to ≈220 nm (image A in the second row of Figure 3). It is seen that some spherical Ba₂LaF₇ crystals of ≈6 nm are uniformly precipitated from the glass matrix. HRTEM image B is obtained from the black-dashed circle of image A. The interplanar distances between the adjacent fringes are determined to be 0.349 nm and 0.301 nm, which match with the (111) and (200) planes of Ba₂LaF₇ crystals, respectively. SAED photograph C confirms that the flower-like Ba₂LaF₇ are indeed single crystals. The inset in image D indicates that the spherical domains, whose lattice fringes lie in the (111) plane with a *d*-spacing of 0.350 nm, are Ba₂LaF₇ single nanocrystals.

Upon HT at 640 °C (the third row of Figure 3), both flower-like and spherical Ba₂LaF₇ crystals (image A) further grow to the average sizes of ≈260 and 15 nm, respectively. Obviously, two kinds of crystals are separately precipitated in the glass matrix. Most of the spherical Ba₂LaF₇ crystals are populated in some regions, in which they are well separated. These Ba₂LaF₇ crystals grow through the migration of Ba²⁺, La³⁺, and F⁻ ions to the nucleation sites. Thus, the composition of the glass matrix (see the regions around the flower-like crystals) is changed by the depletion of the network modifying ions such as Ba²⁺ and La³⁺, and consequently, the network connectivity of the glass matrix increases. The SAED pattern in image C confirms that the Ba₂LaF₇ crystals are still single crystals after HT. In addition, the HRTEM micrograph (image B) shows a well-defined lattice

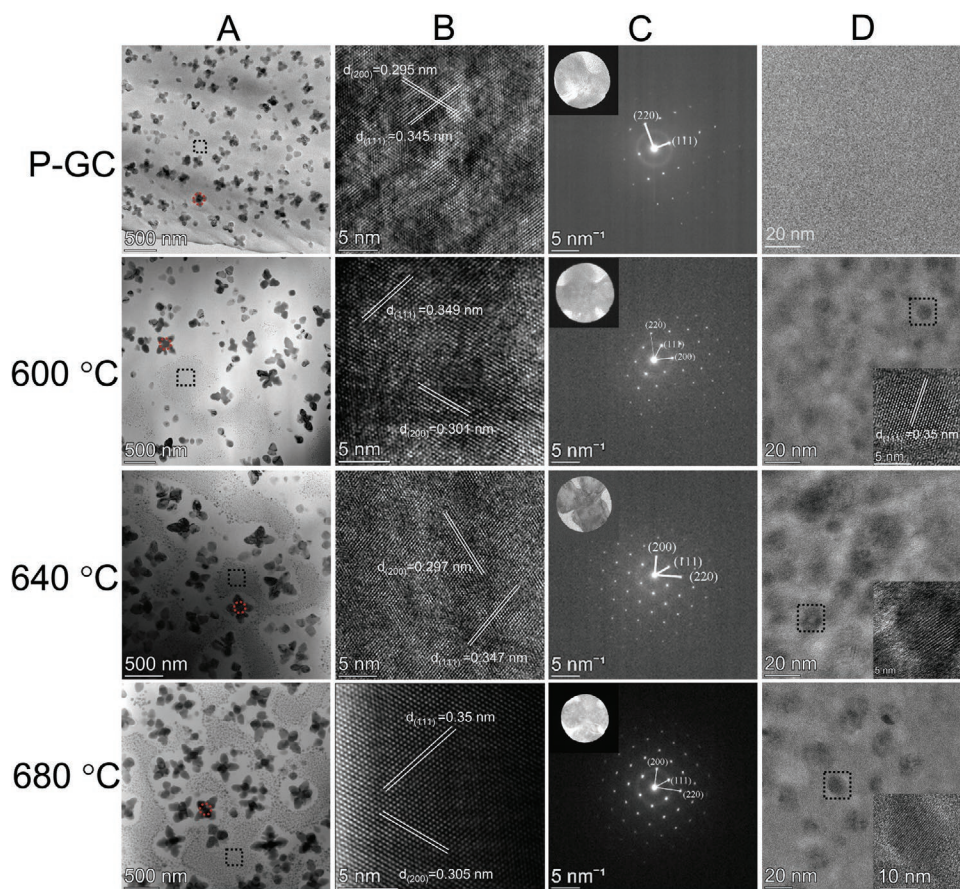


Figure 3. Probing the evolution of crystals during HT and the lattice structure by ACTEM for both P-GC and the heat-treated P-GC samples. A) Overview images (with a scale bar of 500 nm); B) lattice structure; C) electron diffraction of the domains (see inset) selected from red dashed circles in (A). D) Formation of the tiny spherical crystals and their evolution with HT temperature (see the black dashed squares in (A)). Insets: Lattice structure of the tiny spherical crystals selected from black dashed squares in (D).

structure with the interplanar spacings of 0.347 and 0.297 nm in the (111) and (200) planes of Ba_2LaF_7 crystals, respectively.

Upon HT at 680 °C, both the flower-like and the spherical Ba_2LaF_7 crystals grow to ≈ 300 nm and 25 nm, respectively (see image A in the fourth row of Figure 3). Their crystal lattice spacings were measured to be 0.35 and 0.305 nm (image B) in the (111) and (200) planes of Ba_2LaF_7 single crystals (image C), respectively. It is inferred that Ba^{2+} and La^{3+} ions are arranged in an ordered manner, being a typical feature of a single crystal. Image D shows the tiny nanocrystals further growing upon HT.

2.4. Local Structural Analysis of Si, Al, and F Atoms

To reveal the structural evolution during HT, we performed the ^{27}Al , ^{29}Si , and ^{19}F magic angle spinning (MAS) NMR measurements on both P-GC and the heat-treated P-GC samples (Figures 4a–c). It is seen in Figure 4a that ^{27}Al MAS NMR spectra of all the samples feature the main resonance at ≈ 60 ppm, which is attributed to four-coordinated aluminum (Al(IV)). Al^{3+} ions primarily exist in $[\text{AlO}_4]$ tetrahedra besides a minor amount of $[\text{Al}(\text{O},\text{F})_4]$.^[31] The small bumps are the spinning sidebands. After HT, the Al(IV) signal still appears at the same chemical shift as P-GC, suggesting that the coordination

number of Al has no significant change. Note that some Al-F linkages in the interface regions could be replaced by the Al-O linkages upon HT owing to the increasing fraction of Ba_2LaF_7 crystals. This means that the coordination environment of Al could be altered.

Figure 4b illustrates ^{29}Si MAS NMR spectra of P-GC before and after HT. The resonance band at ≈ 86 ppm is ascribed to $Q^{(3)}$ species, where $^{(3)}$ denotes the sum of the numbers of Si-O-Si and Si-O-Al linkages per unit. However, it is hard to find out whether the $Q^{(3)}$ units arise from the Si-O-Si or from Si-O-Al linkages. Thus, the coordination of Si^{4+} does not undergo an obvious change with HT temperature and remains as $Q^{(3)}$.^[32] La^{3+} and F^- play a role as network modifiers, which lowers the network connectivity, thereby facilitating phase separation. It is likely that some La^{3+} ions bond with non-bridging oxygen in the interphase regions, while some reside in the fluoride-rich phase composed of modifying oxides and fluorides, and some participate in the Ba_2LaF_7 crystals.

Figure 4c shows the ^{19}F MAS NMR spectra of both P-GC and the heat-treated P-GC samples. All the spectra exhibit three broad signals at ≈ -12 , -142 , and -185 ppm, which are denoted as F1, F2, and F3, respectively.^[31] The ratio of F1/F3 increases with increasing HT temperature owing to the increasing fraction of Ba_2LaF_7 crystals. F1 signal can be assigned to the F in

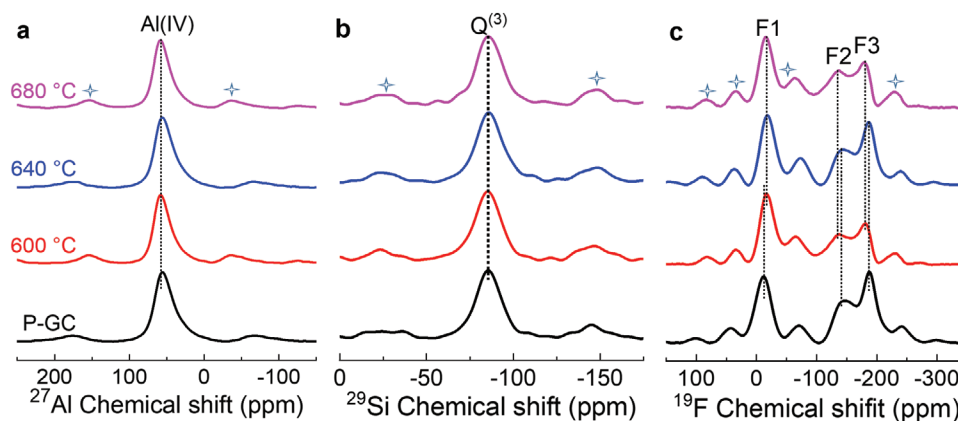


Figure 4. Structure characterizations by MAS NMR. a) ^{27}Al , b) ^{29}Si , and c) ^{19}F spectra of P-GC and the P-GC samples heat-treated at 600, 640, and 680 °C for 4 h. Stars: spinning sidebands.

the La–F–Ba linkage.^[33] Both F2 and F3 signals are related to F species involved in the F–Al linkages of Al–F–Al and Na–F–Al, respectively.^[34,35] Upon HT, the F1 resonance shifts from –12 to –18 ppm, indicating that some of the F ions participate in the formation of the Ba_2LaF_7 crystals, rather than stay in the glass matrix.^[36]

2.5. Origin of the Transparency and Luminescence Enhancement

To explore the origin of the increase of transmittance with HT temperature, we measured the n of both the P-GC sample and the heat-treated ones at different wavelengths (Figure S5a, Supporting Information). It is clearly seen that HT has led to a decrease in n values (Table S5, Supporting Information). This means that the n values of the remaining glass matrix are lowered since that of the Ba_2LaF_7 crystal is constant. n is proportional to the density of the samples,^[37,38] and hence the density exhibits the same variation trend with HT temperature as the n trend (Figure S5b, Supporting Information).

Figure 5a illustrates n_d values at the wavelength of 588 nm and the n_d difference (Δn_d) between the studied samples and the pure Ba_2LaF_7 crystals for comparison. It is seen that Δn_d decreases with increasing HT temperature.^[39] When the

P-GC sample was heat-treated at 680 °C for 4 h, its n_d (1.5459) approaches that of Ba_2LaF_7 crystals ($\approx 1.54@588\text{ nm}$), and consequently, the light scattering of the sample is greatly suppressed.^[40] Hence, this sample displays the highest transmittance. This is opposite to the trend for traditional GCs, where Δn_d increases with increasing HT temperature.

To clarify the origin of the n trend with HT temperature, we performed an EDS-elemental mapping analysis on both Ba_2LaF_7 crystals and the remaining glass matrices. Both the High-Angle Annular Dark Field transmission electron microscope (HAADF-STEM) images of Ba_2LaF_7 crystals and the EDS-element mapping images of Ba, La, and F atoms are shown in Figure 6. The EDS-element mapping images for other types of atoms for P-GC and the three heat-treated P-GC samples are displayed in Figures S6–4, (Supporting Information), respectively. It is seen that the sizes of both the flower-like Ba_2LaF_7 crystals and the small spherical Ba_2LaF_7 crystals increase with HT temperature, and the concentrations of Ba, La, and F during HT also increase. Some Ba^{2+} and nearly all the La^{3+} and F^- diffuse from the glass matrix to both the existing flower-like Ba_2LaF_7 single-crystals and the small spherical Ba_2LaF_7 nanocrystals with increasing HT temperature. As a result of the escape of La^{3+} ions from the glass phase, the n of the sample becomes lower, since La^{3+} ions are the main contributor to the n of glass.^[41]

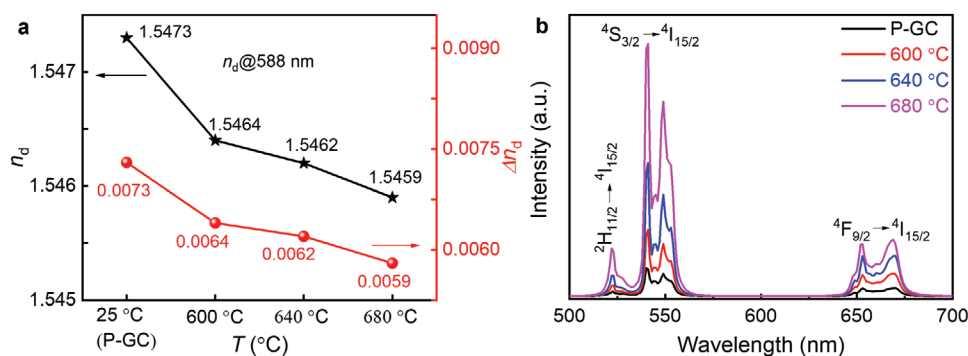


Figure 5. Effect of the HT temperature on the n and UC luminescence of P-GC. a) n_d at the wavelength of 588 nm (black star symbols) and the Δn_d between the studied samples and the Ba_2LaF_7 crystallites (red sphere symbols). Error range of n_d : ± 0.0001 . b) UC luminescence spectra obtained by using the 980 nm laser diode for the four studied samples.

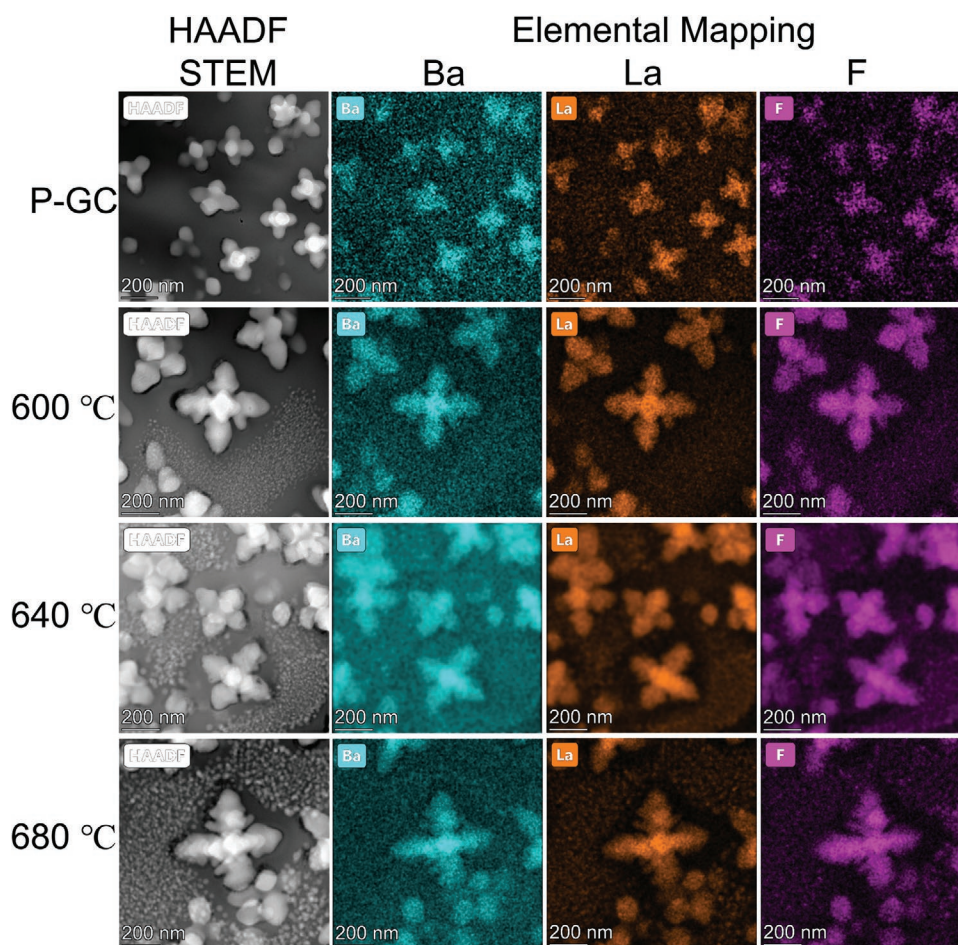


Figure 6. Effect of the HT temperature on the distribution of the elements around the crystals. Micrographs of P-GC and the heat-treated P-GC samples obtained by the HAADF-STEM (see the first column); EDS-mapping images of the elements: Ba, La, and F (see the second, third, and fourth columns, respectively).

Figure 5b shows the UC emission spectra of both P-GC and the heat-treated P-GC samples under the 980 nm laser diode (LD) excitation. Compared to P-GC, the heat-treated P-GC samples exhibit much stronger UC luminescence arising from the transitions ${}^2\text{H}_{11/2} \rightarrow {}^4\text{I}_{15/2}$ (523 nm), ${}^4\text{S}_{3/2} \rightarrow {}^4\text{I}_{15/2}$ (541 and 548 nm), and ${}^4\text{F}_{9/2} \rightarrow {}^4\text{I}_{15/2}$ (653 and 668 nm) of Er^{3+} . This enhancement can be attributed to the following three factors. First, only a small portion of Er^{3+} and Yb^{3+} ions are present in Ba_2LaF_7 crystals in P-GC (Figure S6-1, Supporting Information), but most of them exist in the glass matrix. Since the glass matrix possesses higher phonon energy ($1200\text{--}1300\text{ cm}^{-1}$) than the crystals (270 cm^{-1}), the nonradiative relaxation rate of Er^{3+} and Yb^{3+} in the former is higher than that in the latter.^[25] Hence, the UC luminescence of the P-GC sample is weaker than that of the heat-treated P-GC samples. Second, both the content of Ba_2LaF_7 crystals and the transmittance of the studied samples increase with the HT temperature, and thus, UC luminescence is enhanced by lowering light scattering. Third, as the concentrations of Er^{3+} and Yb^{3+} ions in Ba_2LaF_7 crystals increase with HT temperature, the distance between Er^{3+} and Yb^{3+} in Ba_2LaF_7 crystals becomes shorter, leading to an increased probability of energy transfer between Er^{3+} and Yb^{3+} ions, and thereby to the enhancement of the UC luminescence. The UC luminescence

of the studied P-GC is four times higher than that of the traditional GC (Figure S7a, Supporting Information).^[25] Upon HT at $680\text{ }^\circ\text{C}$ for 4 h, the UC luminescence intensity is increased by ≈ 23 times compared with the traditional GC. Thus, the studied P-GC is an excellent starting candidate for enhancing UC luminescence by proper HT.

3. Conclusion

We prepared a novel type of functional glass ceramics via melt-quenching, that is, the translucent $\text{Er}^{3+}\text{-Yb}^{3+}$ doped oxyfluoride P-GC containing 200 nm sized flower-like Ba_2LaF_7 single-crystals. Interestingly, the transmittance of P-GC increases upon HT above T_g , and this is in contrast to common sense. Normally, HT leads to the growth of crystals, as well as to the formation of new Ba_2LaF_7 nanocrystals, thereby lowering the transmittance of glass-ceramics. This anomalous phenomenon is attributed to the fact that the n of the residual glass matrix approaches that of Ba_2LaF_7 crystals via HT, and thereby light scattering is minimized. The mechanism of both crystal formation and growth was revealed by performing XRD, TEM, and SEM analyses. The structural evolutions in the glass-ceramic during HT have

been probed by NMR and TEM mapping. We found that HT can enhance not only the light transmittance, but also the UC luminescence of the studied glass-ceramic systems.

4. Molecular Dynamics Simulation Section

The structure of the precursor glass (PG) was simulated by using MD simulations via the DL POLY 2.20 package developed at Daresbury Laboratory in the UK with a set of partial charge pairwise potentials with the form of Buckingham that has been successfully used in investigating the structures and phase separation of several oxyfluoride glass systems.^[31] In this study, we used La³⁺ ions to represent other rare earth ions such as Er³⁺ and Yb³⁺ ions hence the simulated glass has the composition of 45SiO₂-15Al₂O₃-12Na₂O-21BaF₂-8.5LaF₃ (mol%). The input density (g cm⁻³), as well as the simulation cell dimension and final density after equilibrium, were listed in Table S6 (Supporting Information). The initial density was theoretically calculated and starting atom's positions were randomly generated.^[31] After generating the simulation bulk with atoms randomly distributed, the simulation bulk was heated to 6000 K and then cooled down to 300 K with a nominal cooling rate of 5 K ps⁻¹. The NVT and NVE ensembles were applied during this simulated melt and quench process at each temperature interval during cooling. At 300 K, constant pressure relaxation with the NPT ensemble was used to allow the system to relax to its equilibrium volume. This is followed by NVE relaxations to generate configurations for the final structural analysis. Further details of MD simulations of oxyfluoride glasses can be found in their recent papers.^[3,29,42]

5. Experimental Section

The precursor glass with the composition (mol%) of 45SiO₂-15Al₂O₃-12Na₂O-21BaF₂-7LaF₃-0.5ErF₃-1.0YbF₃ was prepared by a melting-quench method. 20 g of the powdered mixture was melted in an electric furnace in the air at 1450 °C for 45 min, and quickly cast onto a heating plate at ≈300 °C. Afterward, to remove the permanent stress, the as-cast glass was annealed at 500 °C for 8 h and slowly cooled down to room temperature inside the furnace. The precursor glass sample contains ≈42 vol.% Ba₂LaF₇ crystals according to the XRD (see Figure S1a, Supporting Information), and thus was denoted as the P-GC. P-GC was cut into four small pieces of the same size and polished for both HT and property characterizations. To investigate the effect of HT on both the glass transition and the first crystallization behaviors of P-GC, the P-GC samples were heat-treated at 600, 640, and 680 °C for 4 h, respectively.

DSC (NETZSCH STA 449F3 Jupiter) measurements were carried out on both P-GC and the heat-treated P-GC samples in the temperature range from room temperature to 900 °C at the upscan rate of 10 °C min⁻¹ in nitrogen. To study its crystallization kinetics and thermodynamics, P-GC was subjected to four DSC up- and downscan cycles. For each cycle, the authors chose five maximum scanning temperatures ($T_{\text{scan-max}}$) in the range between the T_g and the temperature close to that of the first broad but shallow crystallization peak (T_{p1}) (see Figure S1b, Supporting Information). Specifically, $T_{\text{scan-max}}$ was chosen to be 580, 600, 620, 640, and 660 °C. For each cycle, the sample was upscanned to $T_{\text{scan-max}}$ and subsequently cooled down to room temperature. XRD measurements were performed to identify the crystallization phase by a PANalytical diffractometer, operated at 40 kV and 40 mA, with Cu-K α ($\lambda = 1.5406 \text{ \AA}$) radiation during the 2θ range of 10–90° with a step size of 0.013°. The

XRD data for Rietveld refinement of the structure was subjected to TOPAS for handling and refining the step analysis comprehensively, 2θ scan range is 10–90° with an interval of 0.02°. The Raman spectra were acquired using a micro-Raman spectrometer (inVia, Renishaw) in the range of 170 to 1200 cm⁻¹. The sample surface was excited by a 532 nm green HeNe laser for an acquisition time of 10 s. The as-precipitated crystallites in the studied samples were characterized by field-emission SEM (QUANTA 200) at the voltage of 30 kV. Before the SEM measurements, the P-GC sample was etched in 7% HF solution for 25 s, while the heat-treated P-GC samples were etched for 15–20 s. The element compositions were determined by a special ACTEM (FEI Titan Cubed Themis G2 300) equipped with an EDS, HAADF-STEM and the SAED at the voltage of 200 kV. The structure of the P-GC and the P-GC samples heat-treated at 600, 640, and 680 °C for 4 h were characterized by conducting the solid-state NMR experiments (Bruker Avance III HD 500 MHz spectrometer (11.7 T)) at 25 °C. The single-pulse MAS ¹⁹F NMR signals were recorded at a resonance frequency of 470.5 MHz, using a 2.5 mm MAS NMR probe. The spinning rate was 24 kHz, and the 90° pulse length of 2 μ s was used. The relaxation delay of ¹⁹F in all the samples was 4 s. The ¹⁹F chemical shifts were referenced to CFCl₃, using AlF₃ ($\delta = -172.5$ ppm) as a secondary standard. ²⁷Al MAS NMR spectra were obtained at the resonance frequency of 130.2 MHz, operating with a 2.5 mm MAS probe at a spinning rate of 12 kHz. The typical pulse length was 0.7 μ s (10° liquid flip angle). The relaxation delay was 0.5 s for all the samples. The chemical shifts of ²⁷Al were referenced to Al(NO₃)₃ (1 M) aqueous solution. ²⁹Si MAS NMR spectra were acquired at the resonance frequency of 99.3 MHz using a 4 mm MAS probe at a spinning rate of 6 kHz. A spin echo pulse scheme with the $\pi/2$ pulse length of 6 μ s was used to acquire the spectrum. The relaxation delay time of P-GC and heat-treated P-GC samples was set as 300 s. The chemical shifts were referenced to tetrakis(trimethylsilyl) silane standard ($\delta = -9.7$ ppm).

The optical absorption spectra in the wavelength range of 275–800 nm were measured using a Varian Cary 50 spectrophotometer. The n of both P-GC and the heat-treated P-GC samples were measured at various wavelengths by KALNEW Precision Refractometer KPR-2000 at 25 °C. The UC photoluminescence spectra in the wavelength range of 500–700 nm were recorded with a HITACHI F-7000 fluorescence spectrophotometer under the 980 nm laser excitation (excitation power was 0.5 W and the slit was 1 nm). The lifetime measurements were carried out using the method described in Ref. [43] The UC photoluminescence decay curves of both P-GC and the P-GC sample heat-treated at 680 °C for 4 h were recorded by FLSP-980 spectrophotometer (Edinburgh Instruments Ltd., Edinburgh, UK), and the excitation source was 980 nm laser with the frequency of 500 Hz.

Supporting Information

Supporting Information is available from the Wiley Online Library or from the author.

Acknowledgements

This work was supported by the China Scholarship Council (CSC, No. 201808530502), the National Natural Science Foundation of China (No. 51862020), Shandong Province (ZR2020ME025), and the Taishan Youth Scholar Project of Shandong Province (tsqn202103098). The authors are grateful to Dr. Xiaoming Zhang and Dr. Liwei Song for performing TEM measurements, and Jingbo Yu for conducting refractive index and solid-state NMR measurements.

Conflict of Interest

The authors declare no conflict of interest.

Data Availability Statement

The data that support the findings of this study are available from the corresponding author upon reasonable request.

Keywords

crystallization, phase separation, refractive index, translucent and transparent glass-ceramic, up-conversion luminescence

Received: December 13, 2021

Revised: March 11, 2022

Published online: May 11, 2022

-
- [1] P. P. Fedorov, A. A. Luginina, A. I. Popov, *J. Fluorine Chem.* **2015**, 172, 22.
- [2] X. F. Liu, J. J. Zhou, S. F. Zhou, Y. Z. Yue, J. R. Qiu, *Prog. Mater. Sci.* **2018**, 97, 38.
- [3] Z. Fang, Z. Chen, W. Peng, C. Shao, S. Zheng, L. Hu, J. Qiu, B.-O. Guan, *Adv. Opt. Mater.* **2019**, 7, 1801572.
- [4] T. Ouyang, S. Kang, Z. Zhang, D. Yang, X. Huang, Q. Pan, J. Gan, J. Qiu, G. Dong, *Adv. Opt. Mater.* **2019**, 7, 1900197.
- [5] C. Lin, C. Bocker, C. Rüssel, *Nano Lett.* **2015**, 15, 6764.
- [6] R. Deng, F. Qin, R. Chen, W. Huang, M. Hong, X. Liu, *Nat. Nanotechnol.* **2015**, 10, 237.
- [7] S. Lv, M. Cao, C. Li, J. Li, J. Qiu, S. Zhou, *ACS Appl. Mater. Interfaces* **2017**, 9, 20664.
- [8] X. Xu, W. Zhang, D. Yang, W. Lu, J. Qiu, S. F. Yu, *Adv. Mater.* **2016**, 28, 8045.
- [9] Z. Zhao, F. Hu, Z. Cao, F. Chi, X. Wei, Y. Chen, C.-K. Duan, M. Yin, *Ceram. Int.* **2017**, 43, 14951.
- [10] C. F. Bohren, D. R. Huffman, *Absorption and Scattering of Light by Small Particles*, Wiley-VCH, Weinheim **2004**.
- [11] J. Qiu, Q. Jiao, D. Zhou, Z. Yang, *J. Rare Earths* **2016**, 34, 341.
- [12] T. Jiang, W. Qin, D. Zhao, *Mater. Lett.* **2012**, 74, 54.
- [13] F. Wang, J. Wang, X. Liu, *Angew. Chem., Int. Ed.* **2010**, 49, 7456.
- [14] Y. Gao, Y. Hu, D. Zhou, J. Qiu, *J. Eur. Ceram. Soc.* **2017**, 37, 763.
- [15] T. Berthier, V. M. Fokin, E. D. Zanotto, *J. Non-Cryst. Solids* **2008**, 354, 1721.
- [16] Q. Zheng, Y. Zhang, M. Montazerian, O. Gulbitten, J. C. Mauro, E. D. Zanotto, Y. Yue, *Chem. Rev.* **2019**, 119, 7848.
- [17] Y. Yue, R. Von der Ohe, S. L. Jensen, *J. Chem. Phys.* **2004**, 120, 8053.
- [18] Z. Li, D. Zhou, L. R. Jensen, J. Qiu, Y. Zhang, Y. Yue, *J. Am. Ceram. Soc.* **2021**, 104, 4471.
- [19] J. Zhang, L. Longley, H. Liu, C. W. Ashling, P. A. Chater, K. A. Beyer, K. W. Chapman, H. Tao, D. A. Keen, T. D. Bennett, Y. Yue, *Chem. Commun.* **2019**, 55, 2521.
- [20] Z. Li, D. Zhou, Y. Yang, P. Ren, R. Zhu, T. Han, J. Qiu, *J. Alloys Compd.* **2018**, 731, 1044.
- [21] Y. Peng, J. Zhong, X. Li, J. Chen, J. Zhao, X. Qiao, D. Chen, *J. Eur. Ceram. Soc.* **2019**, 39, 1420.
- [22] Q. Liu, Y. Tian, C. Wang, F. Huang, X. Jing, J. Zhang, X. Zhang, S. Xu, *Phys. Chem. Chem. Phys.* **2017**, 19, 29833.
- [23] H. Aguiar, J. Serra, P. González, B. León, *J. Non-Cryst. Solids* **2009**, 355, 475.
- [24] P. González, J. Serra, S. Liste, S. Chiussi, B. León, M. Pérez-Amor, *J. Non-Cryst. Solids* **2003**, 320, 92.
- [25] X. Fan, J. Wang, X. Qiao, M. Wang, J. L. Adam, X. Zhang, *J. Phys. Chem. B* **2006**, 110, 5950.
- [26] B. Park, H. Li, L. R. Corrales, *J. Non-Cryst. Solids* **2002**, 297, 220.
- [27] C. Lin, L. Li, C. Bocker, C. Rüssel, *J. Am. Ceram. Soc.* **2016**, 99, 2878.
- [28] C. Massobrio, J. C. Du, M. Bernasconi, P. S. Salmon, *Molecular Dynamics Simulations of Disordered Materials, Springer Series in Materials Science*, Springer International Publishing, Cham, Switzerland **2015**.
- [29] J. Zhao, X. Xu, X. Chen, Q. Xu, Z. Luo, X. Qiao, J. Du, X. Fan, G. Qian, *J. Eur. Ceram. Soc.* **2019**, 39, 5018.
- [30] M. Poulain, *Nature* **1981**, 293, 279.
- [31] J. Zhao, R. Ma, X. Chen, B. Kang, X. Qiao, J. Du, X. Fan, U. Ross, C. Roiland, A. Lotnyk, L. Kienle, X. Zhang, *J. Phys. Chem. C* **2016**, 120, 17726.
- [32] M. M. Smedskjaer, J. C. Mauro, S. Sen, Y. Yue, *Chem. Mater.* **2010**, 22, 5358.
- [33] J. Yu, L. Hu, J. Ren, *Inorg. Chem.* **2021**, 60, 3401.
- [34] X. Zhang, L. Hu, J. Ren, *J. Phys. Chem. C* **2020**, 124, 1594.
- [35] T. J. Kiczanski, J. F. Stebbins, **2002**, 306, 160.
- [36] F. Muñoz, A. De Pablos-Martín, N. Hémono, M. J. Pascual, A. Durán, L. Delevoye, L. Montagne, *J. Non-Cryst. Solids* **2011**, 357, 1463.
- [37] H. N. RITLAND, *J. Am. Ceram. Soc.* **1955**, 38, 86.
- [38] Y. Y. Huang, A. Sarkar, P. C. Schultz, *J. Non-Cryst. Solids* **1978**, 27, 29.
- [39] T. Y. Sun, Y. H. Li, W. L. Ho, Q. Zhu, X. Chen, L. M. Jin, H. M. Zhu, B. L. Huang, J. Lin, B. E. Little, S. T. Chu, F. Wang, *Nat. Commun.* **2019**, 10, 2515.
- [40] T. Wang, B. Liu, Y. Lin, Q. Yang, W. Gao, M. J. Li, J. Qiu, X. Yu, X. Xu, S. F. Yu, *Opt. Lett.* **2020**, 45, 5986.
- [41] A. Masuno, H. Inoue, K. Yoshimoto, Y. Watanabe, *Opt. Mater. Express* **2014**, 4, 710.
- [42] J. Zhao, X. Xu, K. Ren, Z. Luo, X. Qiao, J. Du, J. Qiu, X. Fan, G. Qian, *Adv. Theory Simul.* **2019**, 2, 1900062.
- [43] R. Wang, D. Zhou, J. Qiu, Y. Yang, C. Wang, *J. Alloys Compd.* **2015**, 629, 310.